

Subnanometre-wide electron channels protected by topology

Christian Pauly¹, Bertold Rasche², Klaus Koepf^{3,4}, Marcus Liebmann¹, Marco Pratzner¹, Manuel Richter^{3,4}, Jens Kellner¹, Markus Eschbach⁵, Bernhard Kaufmann¹, Lukasz Plucinski⁵, Claus M. Schneider⁵, Michael Ruck^{2,6}, Jeroen van den Brink^{3,4} and Markus Morgenstern^{1*}

Helical locking of spin and momentum and prohibited backscattering are the key properties of topologically protected states^{1,2}. They are expected to enable novel types of information processing by providing pure spin currents^{3,4}, or fault tolerant quantum computation by using the Majorana fermions at interfaces of topological states with superconductors⁵. So far, the required helical conduction channels used to realize Majorana fermions are generated through the application of an axial magnetic field to conventional semiconductor nanowires⁶. Avoiding the magnetic field enhances the possibilities for circuit design significantly⁷. Here, we show that subnanometre-wide electron channels with natural helicity are present at surface step edges of the weak topological insulator $\text{Bi}_4\text{Rh}_3\text{I}_9$ (ref. 8). Scanning tunneling spectroscopy reveals the electron channels to be continuous in both energy and space within a large bandgap of 200 meV, evidencing its non-trivial topology. The absence of these channels in the closely related, but topologically trivial compound $\text{Bi}_3\text{Pt}_3\text{I}_9$, corroborates the channels' topological nature. The backscatter-free electron channels are a direct consequence of $\text{Bi}_4\text{Rh}_3\text{I}_9$'s structure: a stack of two-dimensional topologically insulating, graphene-like planes separated by trivial insulators. We demonstrate that the surface of $\text{Bi}_4\text{Rh}_3\text{I}_9$ can be engraved using an atomic force microscope, allowing networks of protected channels to be patterned with nanometre precision.

The compound $\text{Bi}_4\text{Rh}_3\text{I}_9$ consists of two types of layers being alternately stacked. One layer, $[(\text{Bi}_4\text{Rh}_3)\text{I}]^{2+}$, exhibits a graphene-like honeycomb lattice formed by rhodium-centred bismuth cubes, as revealed by X-ray diffraction (XRD) (red layer, Fig. 1b) and is a two-dimensional topological insulator (2DTI) according to density functional theory (DFT; ref. 8). Its structure mimics the originally proposed quantum spin Hall insulator in graphene⁹, but with an inverted bandgap being four orders of magnitude larger. The other layer separating the 2DTIs is a $[\text{Bi}_2\text{I}_8]^{2-}$ spacer with a trivial bandgap (blue layer, Fig. 1b). Such a stack of layers has been proposed to be a weak three-dimensional topological insulator (3DTI; ref. 10), as the only alternative of time-reversal protected 3DTIs to the meanwhile intensely studied strong 3DTIs, such as, for example, Bi_2Se_3 (refs 1,2). However, weak 3DTIs remained elusive until DFT results in good correspondence with angle-resolved photoemission spectroscopy (ARPES) data confirmed the synthesized compound $\text{Bi}_4\text{Rh}_3\text{I}_9$ to be one⁸. Theory predicts that weak 3DTIs feature helical

edge states at step edges on the surface that is perpendicular to the stacking direction¹¹. These edge states are topologically protected and immune to backscattering as long as time-reversal symmetry persists. Thus, perfect conduction of these channels with conductivity e^2/h is anticipated^{11,12}. Moreover, partially interfacing these channels with superconductors is predicted to induce Majorana fermions at the rim of the interfacial region⁵.

Scanning tunnelling microscopy (STM) on the cleaved surface of $\text{Bi}_4\text{Rh}_3\text{I}_9$ (that is, the surface perpendicular to the stacking direction) identifies the spacer layer and the 2DTI layer by their different atomic-scale structures (Fig. 1c,d) and their corresponding different step heights (Fig. 1a, inset). The graphene-like honeycomb lattice (Fig. 1c) belongs to the 2DTI layer and exhibits the unit cell size known from XRD (ref. 8), whereas the hexagonally arranged spots in the other layer (Fig. 1d) fit to the iodide ions in the spacer layer $[\text{Bi}_2\text{I}_8]^{2-}$. Combining the STM step height of both layers (1.2 nm) provides a good agreement with the respective layer thickness deduced from XRD (1.25 nm; ref. 8). The 2DTI step edges are mostly zigzag terminated (Fig. 1e, inset) with a few kinks and a few adsorbates on top (Fig. 1e), the latter probably due to remaining iodide ions from the spacer layer (Methods).

Figure 1f shows the locally measured differential conductivity $dI/dV(V)$, known to represent the local density of states (LDOS; ref. 13), as recorded on the 2DTI layer (red curve), on the spacer layer (blue curve) and at the step edge (grey curve). On the 2DTI layer, we find a gap between $V = -180$ mV and $V = -360$ mV (the remaining intensity within this gap is explained in Methods). This is in excellent agreement with the gap measured by ARPES (ref. 8) at -170 to -370 meV below the Fermi level E_F . Importantly, there is a strong dI/dV intensity within this 2DTI gap if measured at the step edge. This indicates the edge state. The peak maximum is in the lower part of the bandgap, in accordance with the dispersion from tight-binding calculations¹⁴. A larger gap is revealed for the spacer layer, as expected. These properties are present on all areas of the sample with slightly different intensity distributions, which are attributed to different local chemistry or to a different density of states of the probing tip.

Figure 1h shows a spatially resolved dI/dV map corresponding to the topography of Fig. 1g and measured at a sample voltage within the bandgap of the 2DTI. Bright stripes at all step edges, mostly being about 15° off from the zigzag direction, indicate the presence of an edge mode, as also found on all other step edges of the 2DTI layer.

¹II. Institute of Physics B and JARA-FIT, RWTH Aachen University, D-52074 Aachen, Germany. ²Department of Chemistry and Food Chemistry, TU Dresden, D-01062 Dresden, Germany. ³Leibniz Institute for Solid State and Materials Research, IFW Dresden, PO box 270116, D-01171 Dresden, Germany. ⁴Department of Physics, TU Dresden, D-01062 Dresden, Germany. ⁵Peter Grünberg Institute PGI-6, Forschungszentrum Jülich, D-52425 Jülich, Germany. ⁶Max Planck Institute for Chemical Physics of Solids, D-01187 Dresden, Germany. *e-mail: mmorgens@physik.rwth-aachen.de

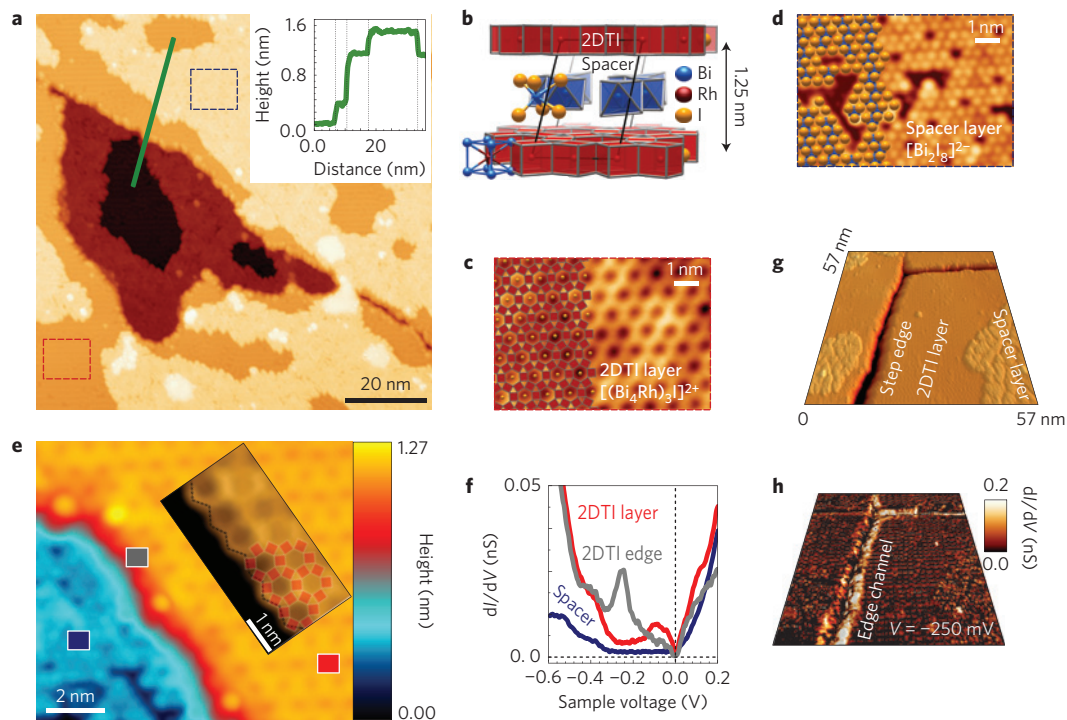


Figure 1 | Identification of the edge state. **a**, STM image of cleaved $\text{Bi}_{14}\text{Rh}_3\text{I}_9$ ($V = 1\text{ V}$, $I = 100\text{ pA}$). Inset: height profile along the green line. **b**, Atomic polyhedron model of $\text{Bi}_{14}\text{Rh}_3\text{I}_9$ as deduced from XRD (ref. 8). **c,d**, Zoomed-in view of the red (**c**) and blue (**d**) dashed boxes in **a**, showing the two different layers. The atomic model structure is overlaid (colour-coded as in **b**). In **c**, $V = 1.5\text{ V}$, $I = 100\text{ pA}$, and in **d**, $V = -1.3\text{ V}$, $I = 100\text{ pA}$. **e**, STM image with the step edge of a 2DTI layer ($V = 0.8\text{ V}$, $I = 100\text{ pA}$). Inset: zoomed-in view of the step edge region with an overlaid honeycomb lattice revealing the zigzag termination (dotted lines are guides to the eye). **f**, $dI/dV(V)$ spectra taken at the positions marked in **e** by the correspondingly coloured squares ($V_{\text{stab}} = 0.8\text{ V}$, $I_{\text{stab}} = 100\text{ pA}$, $V_{\text{mod}} = 4\text{ mV}$). Notice the linearly vanishing dI/dV intensity around E_F , which is attributed to a two-dimensional Coulomb gap of Efros-Shklovskii type³⁴. **g,h**, STM and dI/dV images, respectively, within the 2DTI bandgap of a region with step edges of the 2DTI layer ($V = -250\text{ mV}$, $I = 100\text{ pA}$, $V_{\text{mod}} = 4\text{ mV}$). A strong dI/dV intensity appears at the step edges, being on average different on the right (0.1 nS) and the left (0.07 nS), most probably due to the different stacking of the two step edges with respect to the underlying spacer layer $[\text{Bi}_2\text{I}_8]^{2-}$ caused by the crystal structure²⁶.

Another example of the edge state is shown in Fig. 2a, where its Bloch-type character appears as an oscillation with unit cell periodicity along the zigzag direction (Fig. 2c). A profile line across the edge state exhibits a full-width at half-maximum (FWHM) of only 0.83 nm (Fig. 2b). This is an upper limit due to possible convolution effects with the tip shape. Thus, the edge state is confined to a single unit cell (width: 0.92 nm ; ref. 8), as predicted by tight-binding calculations¹⁴. Such a width is much smaller than for edge states of the buried 2DTI made of HgTe quantum wells (edge state width: $\sim 200\text{ nm}$; refs 12,15), implying the possibility of much smaller devices. Theory predicts that the helical conduction remains robust, mostly for step edge heights containing any number of exposed stacks, and is even stabilized by disorder^{16–20}, where it should be noted that for an even number of stacks a finite size gap can open¹¹. Thus, simply scratching the surface tends to induce one-dimensional electron channels with a robust conductivity of at minimum e^2/h (ref. 18). The first step in that direction is shown in Fig. 2d. Scratches roughly three layers deep are produced by atomic force microscopy (AFM). The distances between the centres of scratches are well below 100 nm and the edge channels are partly separated by only 25 nm . To make such networks operational, it is necessary to move the non-trivial bandgap to E_F . This may be achieved by surface doping (for example, by iodine), recalling that the calculated bulk position of E_F is already within the non-trivial bandgap⁸. DFT slab calculations further reveal n-type doping of the cleaved surface as observed experimentally⁸.

Next, we investigate whether the edge state covers the whole non-trivial bandgap, as predicted by topology. Figure 2e is a colour-coded representation of the energy-dependent LDOS across the step edge.

It reveals a pronounced edge state intensity throughout the whole non-trivial bandgap and slightly weaker intensity even in the energy region below, as expected from tight-binding calculations¹⁴.

This characteristic has been found for all ten probed step edges with lengths from 6 nm to 40 nm . Figure 3a,b shows another example of a 2DTI step edge, again with an extremely narrow edge state running along the edge and being pushed around kinks (Fig. 3a). The edge state intensity is visible along the whole edge at all energies within the bandgap (Fig. 3b, see also Supplementary Movie) and again weaker even at energies below (-400 mV , -450 mV).

Moreover, it shows that intensity fluctuations of the edge state along the edge are small (except at energies below the gap), as expected for the prohibited backscattering. To sustain this assumption, the electron wavelength as deduced from tight-binding calculations¹⁴ $\lambda_{\text{tight-binding}}$ is added to Figs 2a and 3a. Obviously, there is no structure with periodicity $\lambda_{\text{tight-binding}}/2$ (that is, no standing electron waves), in remarkable contrast to conventional one-dimensional electron systems, where such oscillations exhibit LDOS intensity oscillations close to 100% (ref. 21).

Notice that edge states barely prone to backscattering have also been observed on some of the step edges of the 2DTI Bi bilayers on $\text{Bi}(111)$ (ref. 22) and $\text{Bi}_2\text{Te}_3(0001)$ (ref. 23), but in both cases the edge states energetically overlap with bulk states.

The topology of the edge state also requires its ubiquity at step edges. Figure 3c shows a case study for a rather disordered step edge. The intensity at the step edge fluctuates strongly, but the $dI/dV(V)$ spectra always reveal fingerprints of the edge state. This becomes clear when zooming in on different regions near the step edge (Fig. 3c(i)–(v)). The spectra on the 2DTI layer in

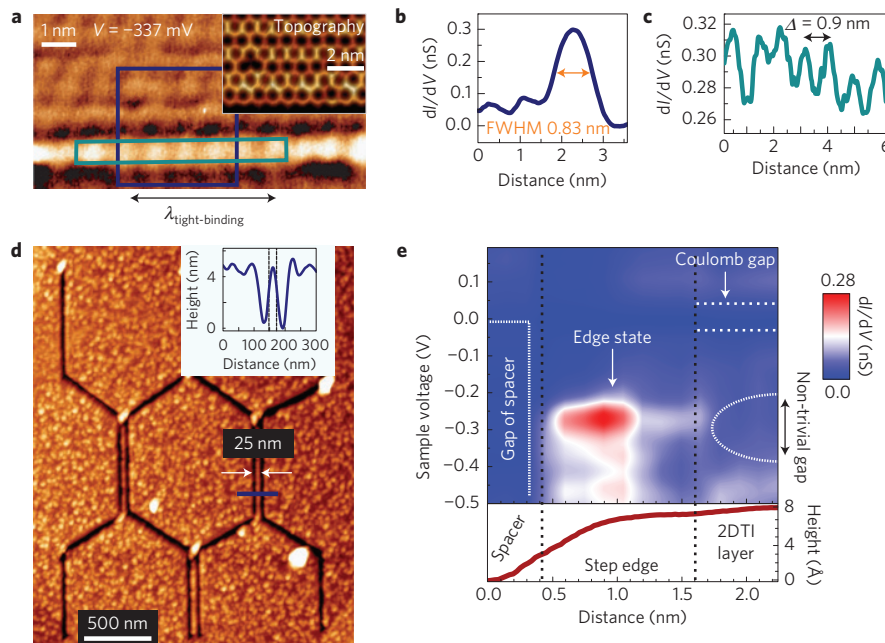


Figure 2 | Edge state properties. **a**, dI/dV image within the bulk bandgap ($V_{\text{stab}} = -337$ mV, $I_{\text{stab}} = 100$ pA, $V_{\text{mod}} = 4$ mV) of the step edge area shown in the inset as a STM image ($V = 0.8$ V, $I = 100$ pA). Rectangles mark the areas of the profile lines shown in **b** and **c**. The double arrow marks the electron wavelength of the edge state at this particular energy as deduced from tight-binding calculations¹⁴. **b**, Profile line perpendicular to the step edge and averaged in the parallel direction over the blue rectangle in **a** with the FWHM of the edge state marked. **c**, Profile line along the step edge taken from the green rectangle in **a** with the marked peak distance corresponding to the size of one unit cell. **d**, AFM image of the $\text{Bi}_4\text{Rh}_3\text{I}_9$ surface after scratching a network of step edges into the surface using a carbon-coated Si cantilever. The profile along the blue line is shown in the inset. **e**, Colour plot of $dI/dV(V)$ spectra taken across the step edge. Three different lateral regions are separated by dotted lines and labelled within the topographic profile below. Different energetic features are marked.

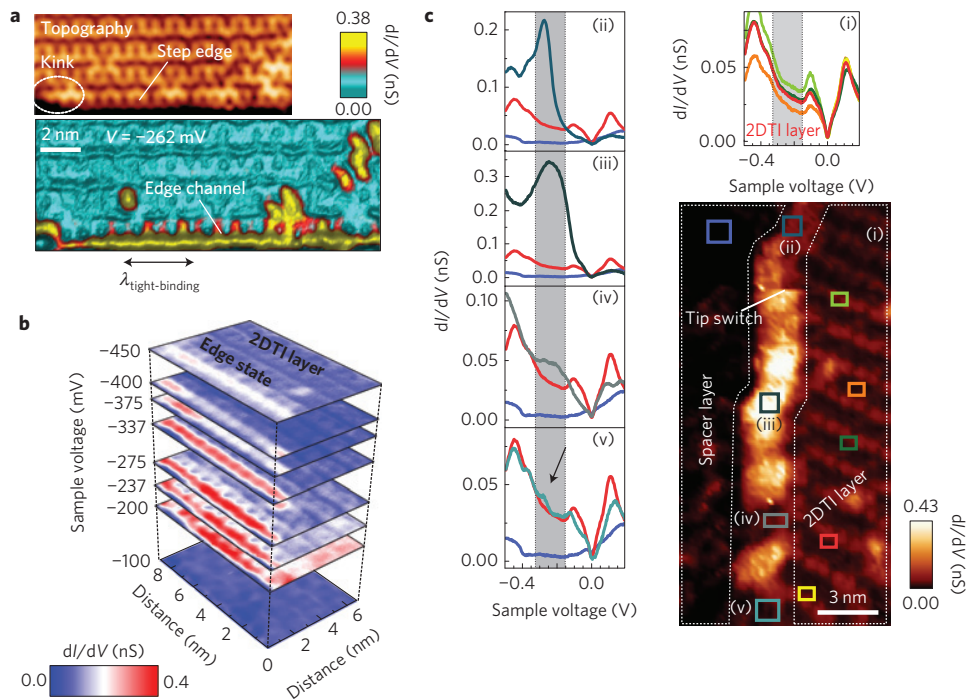


Figure 3 | Non-trivial character of the edge state: continuity in energy and space. **a**, STM image (top, $V = -262$ mV, $I = 100$ pA) and dI/dV image within the bandgap (bottom, $V_{\text{stab}} = -262$ mV, $I_{\text{stab}} = 100$ pA, $V_{\text{mod}} = 4$ mV) of a rather straight step edge. A kink position is marked. The double arrow marks the expected electron wavelength at this particular energy as deduced from tight-binding calculations¹⁴. **b**, Stacked dI/dV images ($I_{\text{stab}} = 100$ pA, $V_{\text{mod}} = 4$ mV) of the area shown in **a** recorded at voltages across the bandgap as marked on the left. **c**, dI/dV image (averaged from $V = -180$ mV to -350 mV, $I_{\text{stab}} = 80$ pA, $V_{\text{mod}} = 4$ mV) including an undulated step edge. The 2DTI layer and spacer layer are labelled and surrounded by dotted lines. The line plots in (i)–(v) show $dI/dV(V)$ spectra ($V_{\text{stab}} = 0.8$ V, $I_{\text{stab}} = 80$ pA, $V_{\text{mod}} = 4$ mV) coloured with respect to their area of origin in the dI/dV image. The spectra in (i) all originate from the 2DTI layer. In (ii)–(v) the blue and red spectra are from the the spacer and the 2DTI layer, respectively, and the other coloured spectra are from the step edge region. Shaded areas in (i)–(v) mark the bulk bandgap as deduced from ARPES.

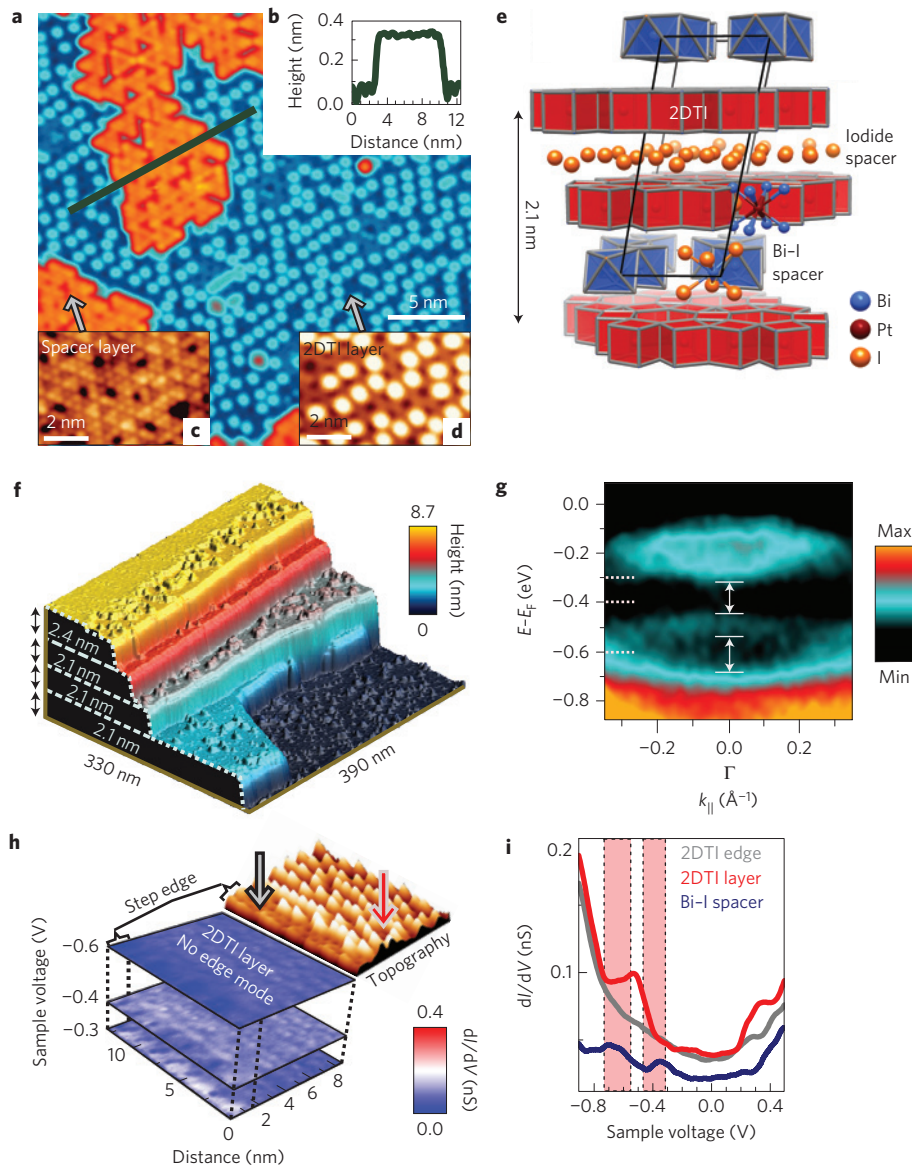


Figure 4 | Absence of a topological edge state in $\text{Bi}_{13}\text{Pt}_3\text{I}_7$. **a**, STM image ($V=1\text{ V}$, $I=100\text{ pA}$) of cleaved $\text{Bi}_{13}\text{Pt}_3\text{I}_7$. **b**, Height profile along the green line in **a**. **c,d**, Atomically resolved images of the two different layers. In **c**, $V=1\text{ V}$, $I=100\text{ pA}$, and in **d**, $V=0.6\text{ V}$, $I=100\text{ pA}$. **e**, Atomic model of $\text{Bi}_{13}\text{Pt}_3\text{I}_7$ as deduced from XRD (ref. 24) with different layers marked. **f**, STM image ($V=1\text{ V}$, $I=100\text{ pA}$) showing step heights of one unit cell (2.1 nm). **g**, ARPES intensity plot ($\hbar\nu=21.2\text{ eV}$); full lines with double arrows mark two bandgaps and dotted lines indicate the energies of the dI/dV plots in **h**. **h**, Stacked dI/dV images ($I_{\text{stab}}=100\text{ pA}$, $V_{\text{mod}}=8\text{ mV}$) of the area shown in the background STM image ($V=0.6\text{ V}$, $I=100\text{ pA}$) and recorded within the bandgaps at the voltages marked on the left, with the same contrast as in Fig. 3b. **i**, Local $dI/dV(V)$ spectra ($V_{\text{stab}}=1\text{ V}$, $I_{\text{stab}}=100\text{ pA}$, $V_{\text{mod}}=8\text{ mV}$) recorded at the positions marked by arrows in **h** and on the insulating spacer layer. Bandgaps deduced from ARPES are marked in red.

region (i) are flat within the bandgap region, with slightly different intensities in different regions due to a variation in coupling to the underlying stripes of the spacer layer, as deduced by comparison with DFT calculations (see Supplementary Section 1). Comparing these spectra with the spectra from most parts of the step edge, for instance region (iii), shows a strong peak indicating the edge state. The sharpness of the peak depends on details of the tip; for example, it appears sharper in region (ii), which is measured after a tip switch. Zooming into an area of small edge state intensity, region (iv), located around a kink position (see topography in Supplementary Section 1), reveals the same peak, but a factor of ten lower in intensity, indicating a smaller coupling of the edge state to the tunnelling tip. Moreover, the edge state intensity is pushed to the right—that is, it moves around the obstacle, as predicted in ref. 16. The size of the peak is even further reduced below a

pair of adsorbates (region (v)), but can still be identified around $V=-270\text{ mV}$ (see arrow). Concluding, we find signatures of a spatially continuous edge state within all investigated step edge areas, pointing to a robust character with respect to disorder, as expected from a topologically protected state.

To further consolidate the topological character of the edge states in $\text{Bi}_{14}\text{Rh}_3\text{I}_9$, we have investigated the very similar system $\text{Bi}_{13}\text{Pt}_3\text{I}_7$, where Rh is replaced by the heavier Pt. The chemical composition is slightly different, such that every second spacer layer is replaced by a single layer of iodide ions²⁴ (see the structural model in Fig. 4e). The honeycomb layer (Fig. 4e) is again a 2DTI, as revealed by DFT, whereas the compound $\text{Bi}_{13}\text{Pt}_3\text{I}_7$ itself is semi-metallic and topologically trivial (DFT results are depicted in Supplementary Section 2). The two different spacers in $\text{Bi}_{13}\text{Pt}_3\text{I}_7$ lead to an alternating coupling between adjacent 2DTI layers,

giving rise to a 'dimerization'. Theoretically it has been shown that such a dimerization can render a topological gap trivial^{17,18} (see Supplementary Information).

STM images of the cleaved surface of $\text{Bi}_{13}\text{Pt}_3\text{I}_7$ (Fig. 4a) again exhibit two different layers, one with hexagonally arranged spots (Fig. 4c), triangularly reconstructed, identified as the insulating $[\text{Bi}_2\text{I}_8]^{2-}$ spacer and the other with a honeycomb structure (Fig. 4d) rendering it the 2DTI. The 2DTI exhibits single atoms on top, most probably remaining iodide ions from the spacers. Interestingly, such iodide ions are absent within the last two unit cells close to the zigzag step edges (Fig. 4h, topography). Pure iodide layers (the other spacer) have not been observed and most step heights (Fig. 4f) cover a complete unit cell of the dimerized layers in the stacking direction (2.1 nm). The band structure of $\text{Bi}_{13}\text{Pt}_3\text{I}_7$ as measured by ARPES at a photon energy $h\nu = 21.2$ eV (Fig. 4g) reveals two band openings around the Γ point. These gaps are found to be trivial in DFT calculations, albeit originating from non-trivial gaps of the 2DTI (Supplementary Section 2). In agreement, STS shows no edge states within these bandgaps (Fig. 4h,i) on any of the ten step edges probed. Notice that the contrast in Fig. 4h is chosen to be identical to Fig. 3b, where the edge state of $\text{Bi}_{14}\text{Rh}_3\text{I}_9$ is clearly apparent. Thus, the dimerized structure of $\text{Bi}_{13}\text{Pt}_3\text{I}_7$, where stacks are built from paired 2DTIs, is a trivial insulator without protected edge states, in accordance with our results from the DFT calculations and general theoretical considerations.

The helical edge states in $\text{Bi}_{14}\text{Rh}_3\text{I}_9$ offers the opportunity to design spin filters⁴ with extremely small footprints compared with 2DTIs in heterostructures¹². Moreover, interfacing with other materials, such as superconductors or magnetic insulators, required for advanced quantum circuitry^{5,7} becomes directly accessible by shadow mask evaporation. In this sense, the discovery of the first weak 3DTI $\text{Bi}_{14}\text{Rh}_3\text{I}_9$ might offer similar advantages to those that graphene does with respect to conventional semiconductor heterostructures²⁵.

Methods

Preparation and growth of $\text{Bi}_{14}\text{Rh}_3\text{I}_9$ crystals. $\text{Bi}_{14}\text{Rh}_3\text{I}_9$ crystals were grown by thermal annealing of a stoichiometric mixture of Bi, Rh and BiI_3 (molar ratio 11:3:3). The starting materials were ground under argon atmosphere in a glovebox. The homogeneous powder was sealed in an evacuated silica ampule and heated to 700 °C in a tubular furnace at a rate of approximately 600 K h⁻¹. Fast cooling to 420 °C (−4 K min⁻¹) and then slow cooling to 365 °C (−1 K h⁻¹) followed instantaneously. After three days the ampule was quenched in water. A more detailed description can be found in ref. 26. Exfoliation of the material, for example, by the Scotch tape method on SiO_2 , is in principle possible, but so far the transport properties related to the topological edge states have not been singled out in exfoliated layers.

Preparation and growth of $\text{Bi}_{13}\text{Pt}_3\text{I}_7$ crystals. $\text{Bi}_{13}\text{Pt}_3\text{I}_7$ crystals were grown by thermal annealing of a stoichiometric mixture of Bi, Pt and BiI_3 (molar ratio 10.67:3:2.33). The starting materials were ground under argon atmosphere in a glovebox. The homogeneous powder was sealed in an evacuated silica ampule and heated to 650 °C in a tubular furnace at a rate of approximately 600 K h⁻¹. Fast cooling to 500 °C (−4 K min⁻¹) and then slow cooling to 380 °C (−1 K h⁻¹) followed instantaneously. After three days the ampule was quenched in water.

Preparation of atomically clean surfaces in ultrahigh vacuum (UHV). The $\text{Bi}_{14}\text{Rh}_3\text{I}_9$ and $\text{Bi}_{13}\text{Pt}_3\text{I}_7$ crystals (~1 mm in diameter) are mounted to a Mo sample holder using a carbon conductive adhesive. Before the STM and ARPES measurements, the samples were cleaved *in situ* at room temperature using a commercial copper tape, leading to atomically flat terraces on the surface, as checked by AFM and STM. The clean sample was immediately transferred into the microscope (STM) or manipulator (ARPES) and cooled down to 6 K or 15 K, respectively. We have checked that the remaining adsorbates at the step edges (Fig. 1e) do not originate from the background pressure. To do this, we varied the background pressure during cleavage and transfer to the STM by a factor of ten. Furthermore, we varied the time between cleavage and transfer to the cryostat, which exhibits an excellent cryogenic vacuum, also by a factor of ten. Neither process changed the density of adsorbates at the step edges. We therefore conclude that these adsorbates arise from the cleavage process itself and originate most probably from the spacer layers.

STM and STS measurements. The microscopic measurements have been performed in a home-built scanning tunnelling microscope in UHV ($p_{\text{phase}} = 10^{-11}$ mbar) at $T = 6$ K (ref. 27). Topographic STM images and dI/dV images are recorded in constant-current mode with voltage V applied to the sample. The $dI/dV(V)$ spectra are recorded after stabilizing the tip at a sample voltage V_{stab} and current I_{stab} before opening the feedback loop. All spectroscopic measurements are carried out using a lock-in technique with a modulation frequency $\nu = 1.4$ kHz and amplitude $V_{\text{mod}} = 4$ mV (8 mV), resulting in an energy resolution $\delta E = \sqrt{(3.3k_B T)^2 + (1.8eV_{\text{mod}})^2} \approx 7$ meV (14 meV) (e , electron charge; k_B , Boltzmann constant)²⁸. To first order, $dI/dV(V)$ is proportional to the local density of states (LDOS) of the actual sample position at energy E with respect to the Fermi level $E_{\text{F,sample}}$ of the sample ($E = E_{\text{F,sample}} + eV$). It is also proportional to the LDOS of the tip at the Fermi level $E_{\text{F,tip}}$ of the tip. However, if the tip LDOS at $E_{\text{F,sample}}$ does not vanish, one gets an additional contribution from the LDOS of the tip at energy E according to $E = E_{\text{F,tip}} - eV$ multiplied by the LDOS of the sample at $E_{\text{F,sample}}$ (ref. 28). Because $E_{\text{F,sample}}$ crosses a bulk band within the 2DTI layer, the latter contribution is also present if the voltage refers to a bandgap of the sample. This explains the remaining dI/dV intensity at voltages corresponding to the 2DTI bandgap. The apparent pseudo-gap at $E_{\text{F,sample}}$ does not remove this contribution due to the finite energy resolution of the experiment²⁸.

AFM experiments. The scratches are produced within a commercial AFM (Bruker) using a carbon-coated silicon cantilever in AFM contact mode at ambient conditions (contact force during scratching: $F = 10^{-6}$ N). The AFM images have been recorded in the tapping mode using the same carbon-coated silicon cantilever (resonance frequency 275.1 kHz, force constant 43 N m⁻¹, oscillation amplitude 30 nm, set point 70%, velocity 2 $\mu\text{m s}^{-1}$).

ARPES measurements. ARPES spectra were measured in UHV ($p_{\text{phase}} = 6 \times 10^{-11}$ mbar) on the cleaved $\text{Bi}_{13}\text{Pt}_3\text{I}_7$ samples kept at 15 K using He I ($h\nu = 21.2$ eV) discharge within a laboratory-based system. The overall energy resolution is 10 meV and the angular resolution is 0.6°. The spectra were recorded within 60 min after cleavage. The fact that the beam spot of the incident light is of the order of the sample size (~1 mm in diameter) causes some background intensity in the ARPES data, probably originating from the carbon conductive adhesive. For the same reason, a slight softening of the bands in the spectra is observable.

Computational details. All band structure calculations were performed with the full-potential local-orbital (FPLO) code²⁹ version 14.00 within the local density approximation (LDA) using the parameterization PW92 according to ref. 30. The Blöchl corrected linear tetrahedron method with a $12 \times 12 \times 6$ k-mesh for $\text{Bi}_{13}\text{Pt}_3\text{I}_7$ and a $12 \times 12 \times 1$ k-mesh for the single 2DTI layer $[\text{Bi}_{12}\text{Pt}_3\text{I}]^{3+}$ was employed. Spin-orbit coupling is treated on the level of the four-component Dirac equation. The following basis states are treated as valence states: Bi: 5s, 5p, 5d, 6s, 7s, 6p, 7p, 6d; Pt: 5s, 5p, 5d, 6s, 6p, 6d, 7s; I: 4s, 4p, 4d, 5s, 6s, 5p, 6p, 5d.

For the band structure calculation of $\text{Bi}_{13}\text{Pt}_3\text{I}_7$, we used the atomic structure as deduced from XRD experiments³⁴. The single 2DTI layer $[\text{Bi}_{12}\text{Pt}_3\text{I}]^{3+}$ was calculated with layers of the type $[Z = 53.625]_4^{1.5-}$ placed above and beneath the $[\text{Bi}_{12}\text{Pt}_3\text{I}]^{3+}$ layer to adjust the charge. The notation $[Z = 53.625]$ means pseudo-atoms with the indicated nuclear charge Z in a virtual crystal approximation. A vacuum layer of 10 Å was added in the c -direction to separate adjacent layers in a three-dimensional supercell geometry. The cell constants and atomic positions were optimized subject to $p6/mmm$ layer symmetry.

The calculation of the topological invariants was implemented following ref. 31, taking into account the fact that the crystals all have an inversion symmetry such that parities of the states at the time-reversal invariant momenta (TRIMs) can be used to calculate the four Z_2 indices $\nu_0; (\nu_1 \nu_2 \nu_3)$ (refs 10,31–33). More details can be found in the Supplementary Information of ref. 8.

Received 12 October 2014; accepted 26 January 2015;
published online 2 March 2015

References

- Qi, X. L. & Zhang, S. C. Topological insulators and superconductors. *Rev. Mod. Phys.* **83**, 1057–1110 (2011).
- Hasan, M. Z. & Kane, C. L. Colloquium: Topological insulators. *Rev. Mod. Phys.* **82**, 3045–3067 (2010).
- Moore, J. E. The birth of topological insulators. *Nature* **464**, 194–198 (2010).
- Brüne, M. *et al.* Spin polarization of the quantum spin Hall edge states. *Nature Phys.* **8**, 485–490 (2012).
- Alicea, J. New directions in the pursuit of Majorana fermions in solid state systems. *Rep. Prog. Phys.* **75**, 076501 (2012).
- Mourik, V. *et al.* Signatures of Majorana fermions in hybrid superconductor–semiconductor nanowire devices. *Science* **336**, 1003–1007 (2012).

7. Alicea, J., Oreg, Y., Refael, G., von Oppen, F. & Fisher, M. P. A. Non-Abelian statistics and topological quantum information processing in 1D wire networks. *Nature Phys.* **7**, 412–417 (2011).
8. Rasche, B. *et al.* Stacked topological insulator built from bismuth-based graphene sheet analogues. *Nature Mater.* **12**, 422–425 (2013).
9. Kane, C. L. & Mele, E. J. Quantum spin Hall effect in graphene. *Phys. Rev. Lett.* **95**, 226801 (2005).
10. Fu, L., Kane, C. L. & Mele, E. J. Topological insulators in three dimensions. *Phys. Rev. Lett.* **98**, 106803 (2007).
11. Yoshimura, Y., Matsumoto, A., Takane, Y. & Imura, K. I. Perfectly conducting channel on the dark surface of weak topological insulators. *Phys. Rev. B* **88**, 045408 (2013).
12. König, M. *et al.* Quantum spin Hall insulator state in HgTe quantum wells. *Science* **318**, 766–770 (2007).
13. Tersoff, J. & Hamann, D. R. Theory of the scanning tunneling microscope. *Phys. Rev. B* **31**, 805–813 (1985).
14. Cano-Cortes, L., Ortix, C. & van den Brink, J. Fundamental differences between quantum spin Hall edge states at zigzag and armchair terminations of honeycomb and ruby nets. *Phys. Rev. Lett.* **111**, 146801 (2013).
15. Zhou, B., Lu, H.-Z., Chu, R.-L., Shen, S.-Q. & Niu, Q. Finite size effects on helical edge states in a quantum spin-Hall system. *Phys. Rev. Lett.* **101**, 246807 (2008).
16. Ringel, Z., Kraus, Y. E. & Stern, A. Strong side of weak topological insulators. *Phys. Rev. B* **86**, 045102 (2012).
17. Fu, L. & Kane, C. L. Topology, delocalization via average symmetry and the symplectic Anderson transition. *Phys. Rev. Lett.* **109**, 246605 (2012).
18. Mong, R. S. K., Bardarson, J. H. & Moore, J. E. Quantum transport and two-parameter scaling at the surface of a weak topological insulator. *Phys. Rev. Lett.* **108**, 076804 (2012).
19. Kobayashi, K., Ohtsuki, T. & Imura, K. I. Disordered weak and strong topological insulators. *Phys. Rev. Lett.* **110**, 236803 (2013).
20. Obuse, H., Ryu, S., Furusaki, A. & Mudry, C. Spin-directed network model for the surface states of weak three-dimensional Z_2 topological insulators. *Phys. Rev. B* **89**, 155315 (2014).
21. Meyer, C., Klijn, J., Morgenstern, M. & Wiesendanger, R. Direct measurement of the local density of states of a disordered one-dimensional conductor. *Phys. Rev. Lett.* **91**, 076803 (2003).
22. Drozdov, I. K. *et al.* One-dimensional topological edge states of bismuth bilayers. *Nature Phys.* **10**, 664–669 (2014).
23. Yang, F. *et al.* Spatial and energy distribution of topological edge states in single Bi(111) bilayer. *Phys. Rev. Lett.* **109**, 016801 (2012).
24. Ruck, M. $\text{Bi}_{13}\text{Pt}_3\text{I}_7$: Ein Subiodid mit einer pseudosymmetrischen Schichtstruktur. *Z. Anorg. Allg. Chem.* **623**, 1535–1541 (1997).
25. Castro Neto, A. H., Guinea, F., Peres, N. M. R., Novoselov, K. S. & Geim, A. K. The electronic properties of graphene. *Rev. Mod. Phys.* **81**, 109–162 (2009).
26. Rasche, B. *et al.* Crystal growth and real structure effects of the first weak 3D stacked topological insulator $\text{Bi}_{14}\text{Rh}_3\text{I}_9$. *Chem. Mater.* **25**, 2359–2364 (2013).
27. Mashoff, T., Pratzner, M. & Morgenstern, M. A low-temperature high resolution scanning tunneling microscope with a three-dimensional magnetic vector field operating in ultrahigh vacuum. *Rev. Sci. Instrum.* **80**, 053702 (2009).
28. Morgenstern, M. Probing the local density of states of dilute electron systems in different dimensions. *Surf. Rev. Lett.* **10**, 933–962 (2003).
29. Koepf, K. & Eschrig, H. Full-potential nonorthogonal local-orbital minimum-basis band-structure scheme. *Phys. Rev. B* **59**, 1743–1757 (1999).
30. Perdew, J. P. & Wang, Y. Accurate and simple analytic representation of the electron-gas correlation energy. *Phys. Rev. B* **45**, 13244–13249 (1992).
31. Fu, L. & Kane, C. L. Topological insulators with inversion symmetry. *Phys. Rev. B* **76**, 045302 (2007).
32. Moore, J. E. & Balents, L. Topological invariants of time-reversal-invariant band structures. *Phys. Rev. B* **75**, 121306 (2007).
33. Roy, R. Topological phases and the quantum spin Hall effect in three dimensions. *Phys. Rev. B* **79**, 195322 (2009).
34. Efros, A. L. & Shklovskii, B. I. Coulomb gap and low-temperature conductivity of disordered systems. *J. Phys. C* **8**, L49–L51 (1975).

Acknowledgements

We acknowledge financial support by the German Science Foundation via Mo 858/13-1, IS 250/1-1 and RI 932/7-1, being part of the Priority Programme 'Topological Insulators' (SPP 1666). C.P. thanks the Fonds National de la Recherche (Luxembourg) for funding. We are indebted to ZIH TU Dresden for the provided computational facilities. We acknowledge helpful discussions with H. Obuse and C. Mudry as well as careful reading of the manuscript by R. McNeil.

Author contributions

C.P. carried out the STM measurements and prepared the first version of the manuscript together with M.M. Material synthesis and XRD analysis were done by B.R. under the supervision of M.Ruck, J.K., M.E. and L.P. performed and analysed the ARPES measurements under the supervision of C.M.S. Band structures have been calculated by B.R. with the support of K.K. and M.Richter. B.K. produced the scratching patterns by AFM. All authors contributed to the data analysis and the writing of the manuscript. M.M. provided the general idea of the experiment and coordinated the project together with C.P.

Additional information

Supplementary information is available in the [online version of the paper](#). Reprints and permissions information is available online at www.nature.com/reprints. Correspondence and requests for materials should be addressed to M.M.

Competing financial interests

The authors declare no competing financial interests.

Copyright of Nature Physics is the property of Nature Publishing Group and its content may not be copied or emailed to multiple sites or posted to a listserv without the copyright holder's express written permission. However, users may print, download, or email articles for individual use.